

QMC-consistent static spin and density local field factors for the uniform electron gas

Aaron D. Kaplan

*Department of Physics, Temple University, Philadelphia, PA 19122**

Carl A. Kukkonen

33841 Mercator Isle, Dana Point, CA 92629†

(Dated: May 16, 2023)

Analytic mathematical models for the static spin (G_-) and density (G_+) local field factors for the uniform electron gas (UEG) as functions of wavevector and density are presented. These models closely fit recent quantum Monte Carlo (QMC) data and satisfy exact asymptotic limits. This model for G_- is available for the first time, and the present model for G_+ is an improvement over previous work. The QMC-computed G_{\pm} are consistent with a rapid crossover between theoretically-derived small- q and large- q expansions of G_{\pm} . These expansions are completely determined by r_s , the UEG correlation energy per electron, and the UEG on-top pair distribution function. We demonstrate their utility by computing uniform electron gas correlation energies over a range of densities. These models, which hold over an extremely wide range of densities, are recommended for use in practical time-dependent density functional theory calculations of simple metallic systems. A revised model of the spin susceptibility enhancement is developed that fits QMC data, and does not show a ferromagnetic instability at low density.

A critical quantity for evaluating the linear response of an interacting uniform electron gas (UEG), or simple metal, are the local field factors (LFFs) $G_{\pm}(r_s, q, \omega)$. The UEG (sometimes called jellium) can be characterized by a Wigner-Seitz density parameter $r_s = [3/(4\pi n)]^{1/3}$ and relative spin-polarization $\zeta = (n_{\uparrow} - n_{\downarrow})/n$, for total density $n = n_{\uparrow} + n_{\downarrow}$. The density (spin-symmetric) LFF $G_+(r_s, q, \omega)$ governs the density-density response $\chi(q, \omega)$ of a many-electron density to a wavevector q - and frequency ω -dependent perturbation via [1]

$$\chi^{-1}(q, \omega) = \chi_0^{-1}(q, \omega) - \frac{4\pi}{q^2} [1 - G_+(r_s, q, \omega)]. \quad (1)$$

$\chi_0(q, \omega)$ is the response function of non-interaction electrons; for the UEG, this is the Lindhard function [2]. Thus G_+ is related to the exchange-correlation kernel f_{xc} of time-dependent density functional theory [3, 4] as $G_+(r_s, q, \omega) = -q^2 f_{xc}(r_s, q, \omega)/(4\pi)$. The spin (antisymmetric) LFF governs the paramagnetic spin-response via [1]

$$\chi_{S_z S_z}^{-1}(q, \omega) = \chi_0^{-1}(q, \omega) + \frac{4\pi}{q^2} G_-(r_s, q, \omega). \quad (2)$$

There exist many approximate expressions of G_+ or f_{xc} , which range from those which are local in space and time [5], nonlocal in space only (as in this work) [6], nonlocal in time only [4, 7], or nonlocal in both space and time [8–10]. However, there are no *realistic* expressions of G_- other than that of Richardson and Ashcroft (RA) [8], which is based on perturbation theory calculations, and

is complicated by typographical errors. As we make extensive comparisons to the RA LFFs, we correct these typographical errors in Supplemental Material Sec. S6. The RA LFFs are presumably most realistic at higher densities typical of simple metals, and less realistic at lower densities.

This work provides flexible, analytic expressions for the static LFFs $G_{\pm}(r_s, q) \equiv \lim_{\omega \rightarrow 0} G_{\pm}(r_s, q, \omega)$ based on known asymptotic limits. Free parameters are then fitted to recent variational diagrammatic quantum Monte Carlo (QMC) calculations [11]. This QMC data covers the region below $q = 2.34k_F$ for $r_s = 1 - 5$ for G_- , but is only available for $r_s = 1$ & 2 for G_+ . The current model of $G_+(r_s, q)$ also more reliably fits older QMC data [12] that covers $r_s = 2, 5$, & 10, but with no data below k_F , than the expression due to Corradini *et al.* [6], and provides accurate predictions of the UEG correlation energy.

Both $G_{\pm}(r_s, q)$ are characterized by a rapid crossover between small- and large- q asymptotics near $q = 2k_F$, with $k_F = (3\pi^2 n)^{1/3}$ the Fermi wavevector. This crossover is likely responsible for the “ $2k_F$ -hump” phenomenon [13, 14]: a maximum in $G_+(q)$ may exist for $q \approx 2k_F$. The presence of a peak can markedly change the properties of phonon dispersion [15], superconducting critical temperatures [16], etc. when using $G_+(q)$ to approximate the LFF of simple metals in TD-DFT. Moreover, explicit inclusion of the spin-dependence of the electronic response via G_- is crucial for describing pairing of electrons in superconducting phases [17, 18]. Thus a realistic approximation of G_- at all possible densities and wavevectors is needed to understand the spin-dependence of the electronic response. Such a model G_- would enable realistic calculations of simple metals using the Kukkonen-Overhauser framework [17] or other theories of linear response.

In this brief paper, we present the formulas for G_+ and G_- for all wave vectors given only the density r_s . The de-

* Currently affiliated with Lawrence Berkeley National Laboratory, Berkeley, CA 94720. ADKaplan@lbl.gov

† kukkonen@cox.net

tails of the curve fitting, asymptotic behavior, and code are given in the Supplemental Material. The formulas may look complex, but are simple to implement computationally; a documented Python implementation is provided in the public code repository [19]. More, the models with optimized parameters can be accessed from PyPI by pip installing “AKCK_LFF.”

The QMC data for both G_+ and G_- closely follow the theoretical asymptotic behavior of varying as q^2 at small q . The coefficients of q^2 are determined by the compressibility and susceptibility sum rules. The QMC data rises somewhat faster than q^2 to about $2k_F$, and then falls rapidly. Theory predicts that the large- q behavior of G_\pm is $B_\pm + Cq^2$. Although B_+ and B_- differ, they are determined by r_s and the on-top pair correlation function. C is the same for both G_\pm . The qualitatively similar behaviors of the LFFs permit us to use the same analytically simple expressions, defined below in Eqs. (3) and (4), to model G_+ and G_- .

The fitting process, partially described below, simply allows the small- q behavior to rise above q^2 , combined with an adjustable exponential cutoff near $2k_F$. This cutoff modulates the transition to the large q asymptotics. The recent QMC data stops at $2.34k_F$, but is consistent with the large- q asymptotic behavior, assuming a simple transition. The following equations completely specify the local field factors.

Let $x \equiv q/k_F$, then we model *both* G_\pm as

$$\begin{aligned} G_j(r_s, q) &= x^2 [A_j(r_s) + \alpha_j(r_s)x^4] H(x^4/16; a_{3j}, a_{4j}) \\ &+ [C(r_s)x^2 + B_j(r_s)] [1 - H(x^4/16; a_{3j}, a_{4j})], \quad (3) \\ \alpha_j(r_s) &= a_{0j} + a_{1j} \exp(-a_{2j}r_s), \quad (4) \end{aligned}$$

where $j = +, -$. The smoothed step function

$$H(y; \beta, \gamma) = \frac{(e^{\beta\gamma} - 1)e^{-\beta y}}{1 + (e^{\beta\gamma} - 2)e^{-\beta y}} \quad (5)$$

is constructed to satisfy three limits: $H(0; \beta, \gamma) = 1$; $H(\gamma; \beta, \gamma) = 1/2$; and $H(\infty; \beta, \gamma) = 0$. While H has no physical basis, it represents a simple and reasonable transition from the low- q behavior of the QMC data to the large- q asymptotics. The a_{ij} parameters are fitted to QMC data.

Equation (3) satisfies the exact small- q expansions (SQEs) of G_\pm , which are identical in structure. For G_+ , this is the compressibility sum rule:

$$\lim_{q \rightarrow 0} G_+(r_s, q) = A_+(r_s)x^2 + \mathcal{O}(x^4), \quad (6)$$

$$A_+(r_s) = -\frac{k_F^2}{4\pi} \frac{\partial^2 e_{xc}^{\text{LDA}}}{\partial n^2}(r_s), \quad (7)$$

with e_{xc}^{LDA} the local-density approximation [20–22] for the UEG exchange-correlation energy density. Unless specified, we use Hartree atomic units, $\hbar = m_e = e^2 = 1$; 1 Hartree energy unit is 2 Rydberg, 27.211386 eV; 1 bohr length unit is 0.529177 Å [23]. The SQE of G_- is the

susceptibility sum rule [1]:

$$\lim_{q \rightarrow 0} G_-(r_s, q) = A_-(r_s)x^2 + \mathcal{O}(x^4), \quad (8)$$

$$A_-(r_s) = -\frac{3\pi}{4k_F} \frac{\partial^2 \epsilon_{xc}^{\text{LSDA}}}{\partial \zeta^2}(r_s, 0). \quad (9)$$

For simple polynomial approximations of $A_\pm(r_s)$ valid for $1 \leq r_s \leq 5$, see Eqs. (6) and (7) of Ref. [11]. $\epsilon_{xc}^{\text{LSDA}}$ is the local spin-density approximation for the UEG exchange-correlation energy per electron, for which we use the Perdew-Wang approximation [22]. The quantity

$$\alpha_{xc}(r_s) \equiv \frac{\partial^2 \epsilon_{xc}^{\text{LSDA}}}{\partial \zeta^2}(r_s, 0) \quad (10)$$

is often called the spin-stiffness [24]. The exchange contribution to the spin-stiffness can be shown to be $\alpha_x(r_s) = -k_F/(3\pi)$ [20, 21, 25].

Equation (3) also satisfies the large- q expansions (LQEs) of G_\pm , again identical in structure. For G_+ , [6]

$$\lim_{q \rightarrow \infty} G_+(r_s, q) = C(r_s)x^2 + B_+(r_s) + \mathcal{O}(x^{-2}), \quad (11)$$

$$C(r_s) = -\frac{\pi}{2k_F} \frac{\partial}{\partial r_s} [r_s \epsilon_c^{\text{LDA}}(r_s)]. \quad (12)$$

The function $B_+(r_s)$ is parameterized as [12]

$$B_+(r_s) = \frac{1 + (2.15)r_s^{1/2} + (0.435)r_s^{3/2}}{3 + (1.57)r_s^{1/2} + (0.409)r_s^{3/2}}. \quad (13)$$

The LQEs of G_- and G_+ are connected as [1, 8, 26, 27]

$$\lim_{q \rightarrow \infty} G_-(r_s, q) = C(r_s)x^2 + B_-(r_s) + \mathcal{O}(x^{-2}), \quad (14)$$

$$B_-(r_s) = B_+(r_s) + 2g(r_s) - 1, \quad (15)$$

i.e., they differ only by the on-top pair distribution function $g(r_s)$, which we approximate as [28]

$$g(r_s) = \frac{1}{2} \frac{1 + 2(0.193)r_s}{\{1 + (0.525)r_s[1 + (0.193)r_s]\}^2}. \quad (16)$$

To fit Eq. (3) for G_\pm , we minimize the deviation from the QMC-computed values of G_\pm , weighted by their corresponding uncertainties. The fitting method is described fully in Supplemental Material Sec. S1. Table I presents fitted parameters a_{ij} and their uncertainties estimated using a bootstrap method. This method is described in the Supplemental Material Sec. S1. We recommend using the full precision of the parameters rather than truncated values based on uncertainty estimates.

Figure 1 compares our fitted G_+ to the data of Ref. [11] and to the older QMC data of Moroni *et al.* [12] for $r_s = 2$. The quality of fit is excellent, lying within the uncertainty of the QMC data at all computed points. The LFF of Corradini *et al.* [6], although fitted to the Moroni *et al.* data, fits it poorly. The LFF developed here, fitted to the Moroni *et al.* data at $r_s = 5$ and 10 only, fits it rather well.

$j =$	$+$ (G_+)	$-$ (G_-)	$-$ (G_-), new α_c
a_{0j}	-0.00451760 ± 0.002	-0.00105483 ± 0.0008	-0.000519869 ± 0.0008
a_{1j}	0.0155766 ± 0.002	0.0157086 ± 0.0006	0.0153111 ± 0.0005
a_{2j}	0.422624 ± 0.2	0.345319 ± 0.05	0.356524 ± 0.05
a_{3j}	3.516054 ± 0.5	2.850094 ± 0.1	2.824663 ± 0.1
a_{4j}	1.015830 ± 0.04	0.935840 ± 0.02	0.927550 ± 0.02

TABLE I. Fit parameters a_{ij} for the model LFFs of Eq. (3) and the estimated uncertainties in the parameters. $i = 1, 2, 3, 4$, and $j = +$ for the G_+ parameters, and $j = -$ for the G_- parameters. The rightmost column uses a revised parameterization for the correlation spin stiffness, described below. Only a_{0-} is sensitive to the choice of α_c , although that may be due to its relatively larger uncertainty.

The Supplemental Material presents further plots of G_+ that demonstrate the quality of fit to the data of Refs. [11, 12] in Figs. S5–S7. Supplemental Figs. S12–S13 show that our model realistically extrapolates to values of r_s for which there are no QMC data. For surface plots of G_+ at metallic densities, see Figs. S16 and S17. At a very high density, $r_s = 0.1$ in Fig. S12, our model and the RA $G_+(r_s, q)$ exhibit very similar behaviors: a simple interpolation between small- and large- q asymptotics with a hump near $2k_F$. At a very low density, $r_s = 100$ in Fig. S13, our model tends to a smooth, hump-free interpolation between the two regimes, but the RA G_+ exhibits likely unphysical oscillations. This latter behavior of RA is consistent with its derivation from perturbation theory.

Moreover, from Figs. 1 and S5–S7, one can see that the QMC data validates the theoretically-derived asymptotic expansions in the small- q limit, and is also consistent with the large- q limit. This is direct validation of the compressibility sum rule. All parameters in $G_+(r_s, q)$ are completely determined by r_s and the UEG correlation energy per electron.

Figure 2 plots the errors in the UEG correlation energies computed using this model and a few common approximations for G_+ . The model of this work systematically overestimates the correlation energies, but makes errors comparable to any of the LFFs presented there. More accurate correlation energies require a frequency-dependent $G_+(r_s, q, \omega)$, such as those of Refs. 8–10. The method of computation is described in Supplemental Material Sec. S5, and a validation of our method using the random phase approximation (RPA, $G_+^{\text{RPA}} = 0$) is given in Supplemental Table S4.

Figure 3 compares our fitted G_- to the Kukkonen-Chen QMC data [11] for $r_s = 4$. The quality of fit is again excellent, lying within the QMC uncertainties at all points. The transition between small- and large- q asymptotics is apparent from Fig. 3(b). Equation (3) avoids the unusual oscillations present in the RA LFF, which is a rational polynomial in q^2 .

Supplemental Figs. S8–S11 demonstrate the high quality of fit to $G_-(r_s, q)$ at other values of $r_s \in \{1, 2, 3, 5\}$. Extrapolations to the same high, $r_s = 0.1$, and low, $r_s = 100$, densities are made in Figs. S14 and S15, respectively. The same conclusions regarding G_+ hold for G_- : our model and RA’s are consistent at high densities,

but RA’s model becomes unphysically oscillatory at low densities. For surface plots of G_- at metallic densities, see Fig. S18.

These figures also show that the QMC data validates the asymptotic expansions of G_- , and thus the spin-susceptibility sum rule. Note that $G_-(r_s, q)$ depends on the parameters of $G_+(r_s, q)$ and the UEG on-top pair distribution function via Eq. (15).

Last, we discuss the accuracy of the PW92 parameterization of the correlation spin stiffness $\alpha_c(r_s)$. It can be observed from either Fig. 4 or Table S3 that the enhancement of the interacting spin-susceptibility χ_s , over the non-interacting spin-susceptibility $\chi_s^{(0)}$ (both per unit volume),

$$\frac{\chi_s}{\chi_s^{(0)}} = \left\{ 1 - \left(\frac{4}{9\pi} \right)^{1/3} \frac{r_s}{\pi} + 3 \left(\frac{4}{9\pi} \right)^{2/3} r_s^2 \alpha_c(r_s) \right\}^{-1}, \quad (17)$$

predicted by PW92 is not consistent with QMC calculations for $r_s > 10$ bohr [11, 29]. For all applications besides low-density jellium, extensive tests have shown PW92 to be robust. In units of the electron spin moment, $\chi_s^{(0)} = 3n/k_F^2$. Recent QMC calculations of $\chi_s/\chi_s^{(0)}$ and of the UEG correlation energy at low densities [30] make it possible to accurately fit α_c directly. The Perdew-Wang model of $\alpha_c(r_s)$ is

$$\alpha_c(r_s) = 2A(1 + \alpha_1 r_s) \times \ln \left[1 + \frac{1}{2A(\beta_1 r_s^{1/2} + \beta_2 r_s + \beta_3 r_s^{3/2} + \beta_4 r_s^2)} \right], \quad (18)$$

where A , β_1 , and β_2 are constrained to ensure the analytic high-density expansion [24]

$$\lim_{r_s \rightarrow 0} \alpha_c(r_s) \approx -\frac{1}{6\pi^2} \ln r_s + 0.035474401. \quad (19)$$

We have recomputed the constant term. To refit α_c , we minimized the deviation from the tabulated values of the susceptibility enhancement [11, 29], and from approximate values of the spin stiffness at low densities [30]. See Supplemental Material Sec. S1 for a description of this method. Table II presents fitted parameters and expansion coefficients. Our parameterization is recommended only for applications where higher precision of

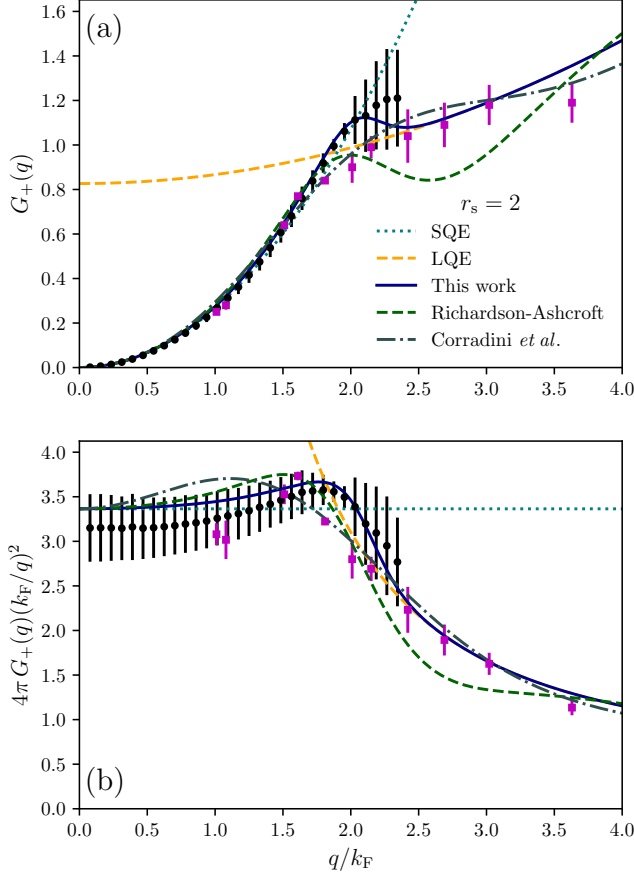


FIG. 1. Comparison of the model G_+ of Eq. (3) (blue, solid line) and Table I with the QMC data of Ref. [11] (black circles with vertical uncertainties) and [12] (magenta squares with vertical uncertainties) for $r_s = 2$. Panel (a) presents G_+ and (b) $4\pi G_+(k_F/q)^2 = k_F^2 f_{xc}(q)$. The latter quantity, essentially the exchange-correlation kernel, is a sensitive test of the fit quality. Also shown are the LFFs of Corradini *et al.* [6] (gray, dash-dotted), which is fitted to the data of Ref. [12], and of RA [8] (green, dashed). The small- q expansion (SQE) of Eq. (6) (teal, dotted) and large- q expansion (LQE) of Eq. (11) (orange, dashed) are also shown.

$\alpha_c(r_s > 10)$ is needed: our model and PW92 appear to differ at most by about 3.3% at $r_s = 18.3$ bohr. We still use the PW92 parameterization of α_c in our model G_- via Eq. (9). Table I also provides model parameters for G_- using the current parameterization of α_c . Consistent with the improvements in α_c , the quality of fit is numerically improved, although the two variants of G_- are visually indistinct.

Consistent with recent QMC-driven analyses of the low-density phases of the UEG [30, 31], our parameterization of α_c yields no divergence in the susceptibility enhancement. The present and PW92 parameterizations of α_c both predict near-divergences in $\chi_s/\chi_s^{(0)}$. Such a divergence would indicate a ferromagnetic instability in the low-density UEG, whereby a transition from the param-

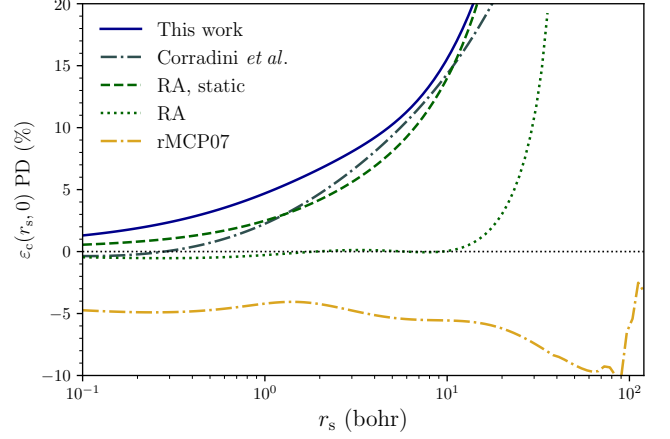


FIG. 2. Percent deviation (PD) from the Perdew-Wang approximation [22] of the UEG correlation energy, using a few common approximations for G_+ . We define the PD as (100%) $[1 - \varepsilon_c^{\text{approx}}/\varepsilon_c^{\text{PW92}}]$. The solid blue curve is computed using Eq. (3) and Table I. The dashed green curve is the static limit of the RA LFF [8], and the dotted green curve is its frequency-dependent form. The dash-dotted gray curve is due to Ref. [6], and the dash-dotted yellow curve to Ref. [10]. The numeric integration for both variants of the RA LFF appears to become unstable for $r_s \gtrsim 45$.

α_c parameter		Expansion coefficient	
A	0.016886864	c_0	-0.016886864
α_1	0.086888870	c_1	0.035474401
β_1	10.357564711	c_2	0.001467281
β_2	3.623216709	c_3	0.005782963
β_3	0.439233491	d_0	0.210976870
β_4	0.411840739	d_1	0.225009568

TABLE II. Left two columns: parameters appearing in Eq. (18) for the correlation spin stiffness, $\alpha_c(r_s)$. Right two columns: expansion coefficients derived using these parameters, such that $\lim_{r_s \rightarrow 0} \alpha_c(r_s) = c_0 \ln r_s - c_1 + c_2 r_s \ln r_s - c_3 r_s + \dots$ and $\lim_{r_s \rightarrow \infty} \alpha_c(r_s) = -d_0/r_s + d_1/r_s^{3/2} + \dots$.

agnetic to ferromagnetic fluid phases is possible. Both Refs. [31] and [30] find that a transition to a Wigner crystal phase occurs before a transition to the ferromagnetic fluid phase.

In summary, this work presents straightforward analytic models of the static density (spin-symmetric) and spin (antisymmetric) local field factors of the uniform electron gas (UEG), which are fitted to recent QMC data [11]. These models hold at an extremely wide range of densities, and the model of G_+ predicts UEG correlation energies with accuracy sufficient to recommend use in practical calculations of simple metallic systems. We have also re-parameterized the correlation spin-stiffness of the UEG using QMC data [11, 29, 30], which shows no transition to a ferromagnetic fluid phase.

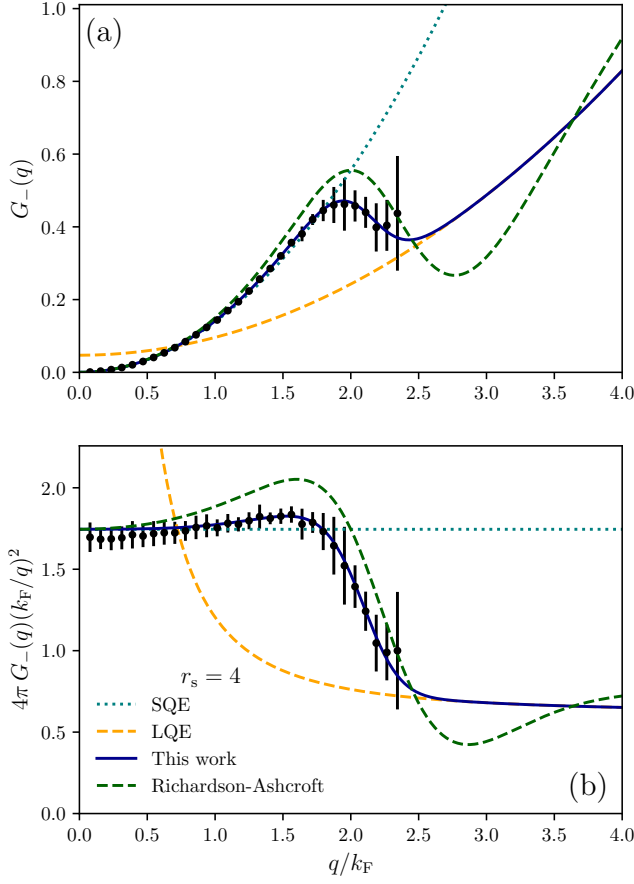


FIG. 3. Comparison of the model G_- of Eq. (3) (blue, solid curve) and Table I with the QMC data of Ref. [11] (black circles with vertical uncertainties) for $r_s = 4$. Panel (a) presents G_- and (b) $4\pi G_-(k_F/q)^2$. The static RA [8] LFF is also shown (green, dashed). The small- q expansion (SQE) of Eq. (8) (teal, dotted) and the large- q expansion (LQE) of Eq. (14) (orange, dashed) are also shown.

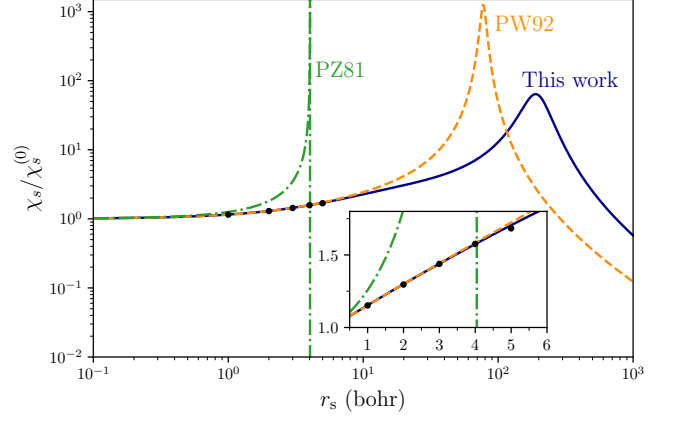


FIG. 4. Susceptibility enhancement $\chi_s/\chi_s^{(0)}$ computed with QMC [11, 29] (black dots with almost imperceptible error bars), using Eq. (17) with the Perdew-Wang (PW92) [22] approximation for α_c (orange, dashed), the re-parameterized form motivated here (blue, solid), or the older expression due to Perdew and Zunger (PZ81) [32] (green, dash-dotted). Although PZ81 includes no explicit information on α_c , it is often used in solid-state and time-dependent density functional calculations. The inset shows the range $0.5 \leq r_s \leq 6$.

ACKNOWLEDGMENTS

A.D.K. thanks Temple University for a presidential fellowship. We acknowledge helpful discussions with John P. Perdew.

-
- [1] G. F. Giuliani and G. Vignale, *Quantum Theory of the Electron Liquid* (Cambridge University Press, Cambridge, 2005).
 - [2] J. Lindhard, Mat. Fys. Medd. Dan. Vid. Selsk. **28**, 1 (1954).
 - [3] E. Runge and E. K. U. Gross, Phys. Rev. Lett. **52**, 997 (1984).
 - [4] E. K. U. Gross and W. Kohn, Phys. Rev. Lett. **55**, 2850 (1985).
 - [5] A. Zangwill and P. Soven, Phys. Rev. A **21**, 1561 (1980).
 - [6] M. Corradini, R. Del Sole, G. Onida, and M. Palumbo, Phys. Rev. B **57**, 14569 (1998).
 - [7] Z. Qian and G. Vignale, Phys. Rev. B **65**, 235121 (2002).
 - [8] C. F. Richardson and N. W. Ashcroft, Phys. Rev. B **50**, 8170 (1994).
 - [9] A. Ruzsinszky, N. K. Nepal, J. M. Pitarke, and J. P. Perdew, Phys. Rev. B **101**, 245135 (2020).
 - [10] A. D. Kaplan, N. K. Nepal, A. Ruzsinszky, P. Ballone, and J. P. Perdew, Phys. Rev. B **105**, 035123 (2022).
 - [11] C. A. Kukkonen and K. Chen, Phys. Rev. B **104**, 195142 (2021).
 - [12] S. Moroni, D. M. Ceperley, and G. Senatore, Phys. Rev. Lett. **75**, 689 (1995).
 - [13] A. W. Overhauser, Phys. Rev. B **2**, 874 (1970), and references therein.
 - [14] K. Utsumi and S. Ichimaru, Phys. Rev. B **22**, 5203 (1980).
 - [15] Y. R. Wang, M. Ashraf, and A. W. Overhauser, Phys. Rev. B **30**, 5580 (1984), and references therein.
 - [16] J. J. Sherron and J. Ruvalds, Phys. Rev. B **34**, 7596 (1986).
 - [17] C. A. Kukkonen and A. W. Overhauser, Phys. Rev. B **20**, 550 (1979).
 - [18] T. Büche and H. Rietschel, Phys. Rev. B **41**, 8691 (1990).
 - [19] View the code repository at https://github.com/esoteric-ephemera/UEG_LFF, or the Python Package Index (PyPI) package at <https://pypi.org/project/AKCK-LFF/>. Both contain usage instructions, CC0 licensing information, and installation instructions.
 - [20] P. A. M. Dirac, Math. Proc. Camb. Phil. Soc. **26**, 376 (1930).
 - [21] W. Kohn and L. J. Sham, Phys. Rev. **140**, A1133 (1965).
 - [22] J. P. Perdew and Y. Wang, Phys. Rev. B **45**, 13244 (1992).
 - [23] We use the most recent NIST CODATA for these values. Refer to <https://physics.nist.gov/cgi-bin/cuu/Value?hr> and <https://physics.nist.gov/cgi-bin/cuu/Value?bohrrada0>.
 - [24] S. H. Vosko, L. Wilk, and M. Nusair, Can. J. Phys. **58**, 1200 (1980).
 - [25] G. L. Oliver and J. P. Perdew, Phys. Rev. A **20**, 397 (1979).
 - [26] G. Niklasson, Phys. Rev. B **10**, 3052 (1974).
 - [27] X. Zhu and A. W. Overhauser, Phys. Rev. B **30**, 3158 (1984).
 - [28] J. P. Perdew and Y. Wang, Phys. Rev. B **46**, 12947 (1992).
 - [29] K. Chen and K. Haule, Nature Commun. **10**, 3725 (2019).
 - [30] S. Azadi and N. D. Drummond, Phys. Rev. B **105**, 245135 (2022).
 - [31] M. Holzmann and S. Moroni, Phys. Rev. Lett. **124**, 206404 (2020).
 - [32] J. P. Perdew and A. Zunger, Phys. Rev. B **23**, 5048 (1981).
 - [33] P. Virtanen, R. Gommers, T. E. Oliphant, M. Haberland, T. Reddy, D. Cournapeau, E. Burovski, P. Peterson, W. Weckesser, J. Bright, S. J. van der Walt, M. Brett, J. Wilson, K. J. Millman, N. Mayorov, A. R. J. Nelson, E. Jones, R. Kern, E. Larson, C. J. Carey, Í. Polat, Y. Feng, E. W. Moore, J. VanderPlas, D. Laxalde, J. Perktold, R. Cimrman, I. Henriksen, E. A. Quintero, C. R. Harris, A. M. Archibald, A. H. Ribeiro, F. Pedregosa, P. van Mulbregt, and SciPy 1.0 Contributors, Nature Methods **17**, 261 (2020).
 - [34] W. H. Press, S. A. Teukolsky, W. T. Vetterling, and B. P. Flannery, Numerical recipes in fortran 77 (Cambridge University Press, Cambridge, 1992) pp. pp. 686–687.
 - [35] M. Lein, E. K. U. Gross, and J. P. Perdew, Phys. Rev. B **61**, 13431 (2000).
 - [36] J. P. Perdew, A. Ruzsinszky, J. Sun, N. K. Nepal, and A. D. Kaplan, Proc. Natl. Acad. Sci. U.S.A. **118**, e2017850118 (2021).

**SUPPLEMENTAL MATERIAL:
QMC-CONSISTENT STATIC SPIN AND DENSITY LOCAL FIELD FACTORS FOR THE UNIFORM
ELECTRON GAS**

CONTENTS		S2. Evaluation of the fit quality at all values of r_s	S9
		A. Static density local field factor	S9
		B. Static spin local field factor	S11
Acknowledgments	6		
		S3. Quality of extrapolation	S13
		A. Static density local field factor	S13
References	6	B. Static spin local field factor	S14
Supplemental Material: QMC-consistent static spin and density local field factors for the uniform electron gas	S7	S4. Surface plots of the local field factors	S15
		S5. Computation of correlation energies	S15
S1. Fitting procedure	S7	S6. Corrected expressions for the Richardson-Ashcroft local field factors	S17

S1. FITTING PROCEDURE

To fit the local field factors (LFFs) G_{\pm} , we performed a least squares fit using the SciPy package [33]. The sum of squared residuals

$$\chi_{\pm}^2 = \sum_{i,j} \left| \frac{G_{\pm}(r_s^{(i)}, q_j) - G_{\pm}^{\text{QMC}}(r_s^{(i)}, q_j)}{\delta G_{\pm}^{\text{QMC}}(r_s^{(i)}, q_j)} \right|^2 \quad (\text{S20})$$

was minimized. G_{\pm}^{QMC} is the LFF computed from QMC, and $\delta G_{\pm}^{\text{QMC}}$ is its uncertainty. For G_+ , we fit to the Kukkonen-Chen [11] data for $G_+(0 \leq q_j/k_F < 2.5)$ at $r_s^{(i)} \in \{1, 2\}$; and to the Moroni *et al.* [12] data for $G_+(1 < q_j/k_F < 4.25)$ at $r_s^{(i)} \in \{5, 10\}$. For G_- , we fit only to the Kukkonen-Chen [11] data for $G_-(0 \leq q_j/k_F < 2.5)$ at $r_s^{(i)} \in \{1, 2, 3, 4, 5\}$.

To estimate uncertainties in the parameters, we use a “bootstrap” method described by Ref. [34]. Suppose we fit to N QMC data points. From these N data points, we construct M artificial data sets whose contents are randomly selected from the true data set, with replacement. We then repeat the least squares fit, using the optimal parameters for the true data set as initial guesses; this appeared to be necessary to stabilize the uncertainty estimators. Call the true, optimized parameters a_i . The parameters from optimization of the k^{th} data set will be called $a_i^{(k)}$. We then compute the mean and variance in the parameters over M synthetic data sets,

$$\bar{a}_i = \frac{1}{M} \sum_{k=1}^M a_i^{(k)} \quad (\text{S21})$$

$$\text{var}(a_i) = \frac{1}{M} \sum_{k=1}^M \left[a_i^{(k)} \right]^2. \quad (\text{S22})$$

The uncertainty in the i^{th} parameter is then estimated as

$$\delta a_i = [\text{var}(a_i) - \bar{a}_i^2]^{1/2}. \quad (\text{S23})$$

In practice, we used $M = 1000$ synthetic data sets, and manually inspected their values as a function of increasing M for stability of the uncertainty estimators.

To fit the correlation spin-stiffness α_c , we performed a least-squares [33] minimization of the objective function

$$\sigma = \sum_i \left| \frac{\tilde{\chi}_{\text{approx}}(r_s^{(i)}) - \tilde{\chi}_{\text{QMC}}(r_s^{(i)})}{\delta \tilde{\chi}_{\text{QMC}}(r_s^{(i)})} \right|^2 + \sum_i \left| \frac{\alpha_c(r_s^{(i)}) - \alpha_c^{\text{QMC}}(r_s^{(i)})}{\delta \alpha_c^{\text{QMC}}(r_s^{(i)})} \right|^2. \quad (\text{S24})$$

r_s	QMC [11, 29]	PW92		This work	
		χ_s/χ_P	PD (%)	χ_s/χ_P	PD (%)
1	1.152(2)	1.153425	0.12	1.153466	0.13
2	1.296(6)	1.299474	0.27	1.299030	0.23
3	1.438(9)	1.442503	0.31	1.439717	0.12
4	1.576(9)	1.583653	0.48	1.575237	-0.05
5	1.683(15)	1.723687	2.39	1.705048	1.30

TABLE S3. Values of the spin-susceptibility enhancement calculated in Refs. [11, 29], here by Eq. (17) using the Perdew-Wang (PW92) parameterization [22] of the UEG correlation energy density, and in this work using a revised parameterization of the Perdew-Wang form. The percent difference (PD) in quantities x and y is defined here as $(200\%)(x - y)/(x + y)$, i.e., the difference of x and y weighted by their average.

$\tilde{\chi}_{\text{QMC}} = \chi_s^{\text{QMC}}/\chi_s^{(0)}$, and $\delta\tilde{\chi}_{\text{QMC}}$ is its uncertainty, for $r_s^{(i)} = 1, 2, 3, 4, 5$. $\tilde{\chi}_{\text{approx}} = \chi_s^{\text{approx}}/\chi_s^{(0)}$ is computed using Eqs. (17) and (18). Using the Perdew-Zunger [32] ansatz for the spin-dependence of the correlation energy,

$$\varepsilon_c(r_s, \zeta) = \varepsilon_c(r_s, 0) + f(\zeta) [\varepsilon_c(r_s, 1) - \varepsilon_c(r_s, 0)], \quad (\text{S25})$$

$$f(\zeta) = \frac{(1 + \zeta)^{4/3} + (1 - \zeta)^{4/3} - 2}{2^{4/3} - 2}, \quad (\text{S26})$$

we have approximated

$$\alpha_c^{\text{QMC}}(r_s) = f''(0) [\varepsilon_c^{\text{QMC}}(r_s, 1) - \varepsilon_c^{\text{QMC}}(r_s, 0)], \quad (\text{S27})$$

$$\delta\alpha_c^{\text{QMC}}(r_s) = f''(0) \left\{ [\delta\varepsilon_c^{\text{QMC}}(r_s, 1)]^2 + [\delta\varepsilon_c^{\text{QMC}}(r_s, 0)]^2 \right\}^{1/2}, \quad (\text{S28})$$

with $\varepsilon_c^{\text{QMC}}$ the accurate correlation energies from Table VI of Ref. [30], and $\delta\varepsilon_c^{\text{QMC}}$ their uncertainties. A few values of the spin susceptibility enhancement predicted by QMC, PW92, and the present work are presented in Table S3.

S2. EVALUATION OF THE FIT QUALITY AT ALL VALUES OF r_s

This section presents figures analogous to Figs. 1 and 3 of the main text, but for the other values of r_s used to fit $G_{\pm}(q)$. For $G_+(r_s, q)$, these are for $r_s \in \{1, 5, 10\}$ in Figs. S5–S7. For $G_-(r_s, q)$, these are for $r_s \in \{1, 2, 3, 5\}$ in Figs. S8–S11.

A. Static density local field factor

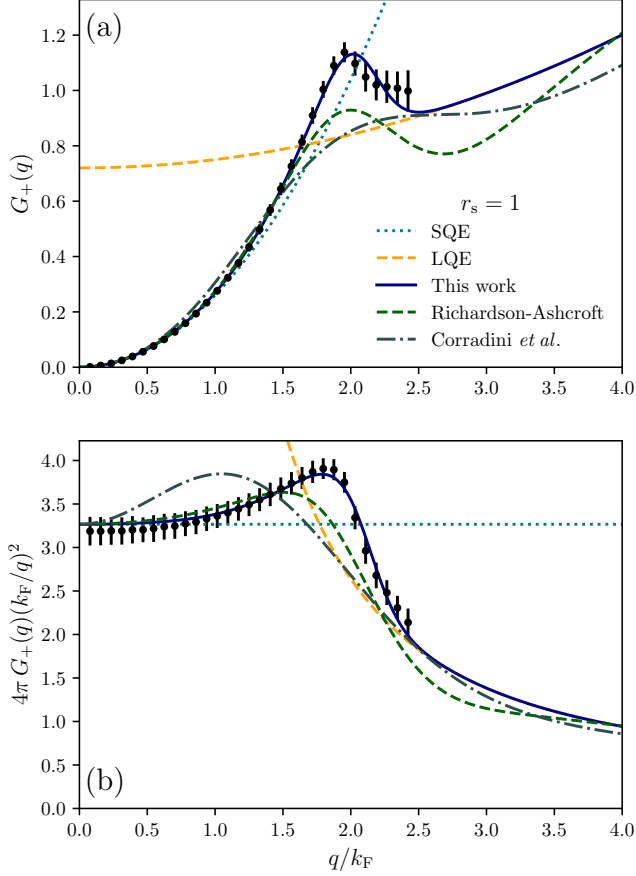


FIG. S5. Comparison of the model G_+ of Eq. (3) (blue, solid curve) and Table I with the QMC data of Ref. [11] (black circles with vertical uncertainties) for $r_s = 1$. Panel (a) presents G_+ and (b) $4\pi G_+(k_F/q)^2 = k_F^2 f_{xc}(q)$. Also shown are the LFFs of Corradini *et al.* [6] (gray, dash-dotted), which is fitted to the data of Ref. [12], and of RA [8] (green, dashed). The small- q expansion (SQE) of Eq. (6) (teal, dotted) and large- q expansion (LQE) of Eq. (11) (orange, dashed) are also shown.

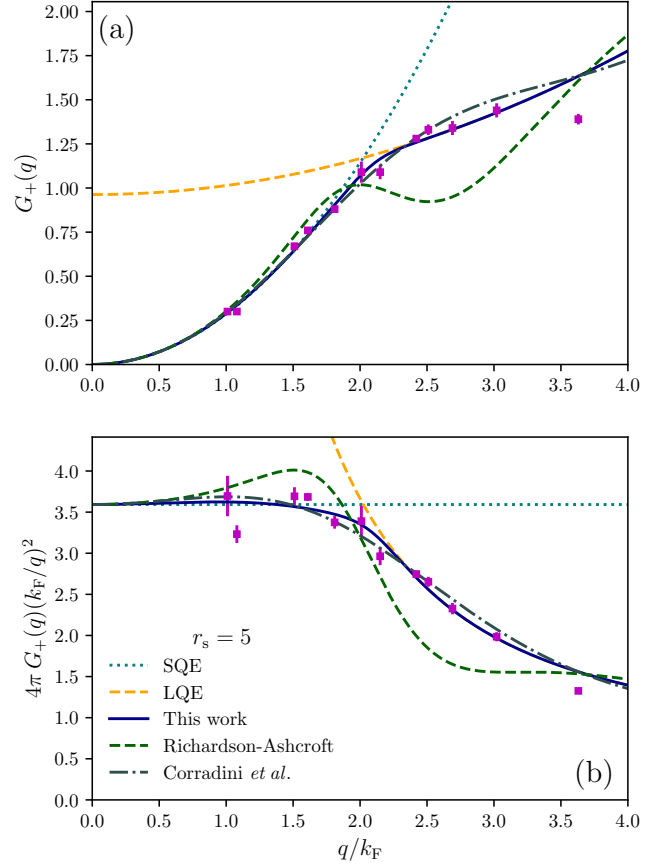


FIG. S6. Comparison of the model G_+ of Eq. (3) (blue, solid curve) and Table I with the QMC data of Ref. [12] (magenta squares with vertical uncertainties) for $r_s = 5$. Panel (a) presents G_+ and (b) $4\pi G_+(k_F/q)^2 = k_F^2 f_{xc}(q)$. Also shown are the LFFs of Corradini *et al.* [6] (gray, dash-dotted), which is fitted to the data of Ref. [12], and of RA [8] (green, dashed). The small- q expansion (SQE) of Eq. (6) (teal, dotted) and large- q expansion (LQE) of Eq. (11) (orange, dashed) are also shown.

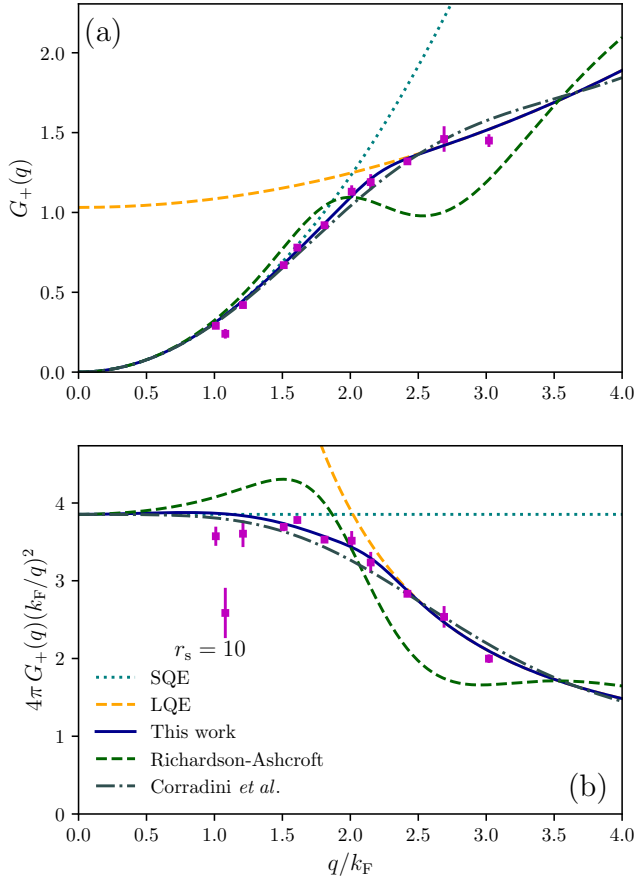


FIG. S7. Same as Fig. S6, but for $r_s = 10$.

B. Static spin local field factor

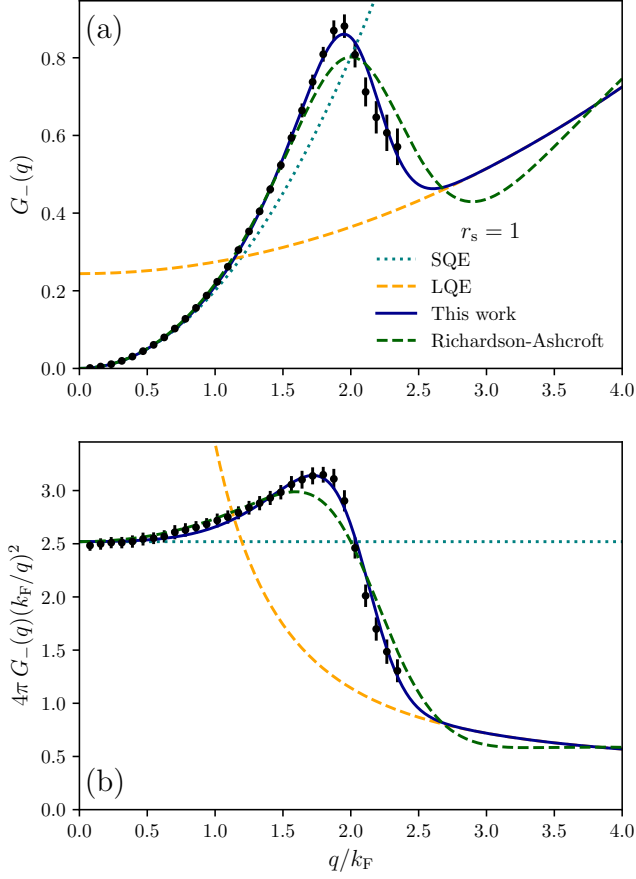


FIG. S8. Comparison of the model G_- of Eq. (3) (blue, solid curve) and Table I with the QMC data of Ref. [11] (black points with vertical uncertainties) for $r_s = 1$. Panel (a) presents G_- and (b) $4\pi G_-(k_F/q)^2 = k_F^2 f_{xc}(q)$. The RA expression for G_- [8] (green, dashed), the small- q expansion (SQE) of Eq. (6) (teal, dotted), and large- q expansion (LQE) of Eq. (11) (orange, dashed) are also shown.

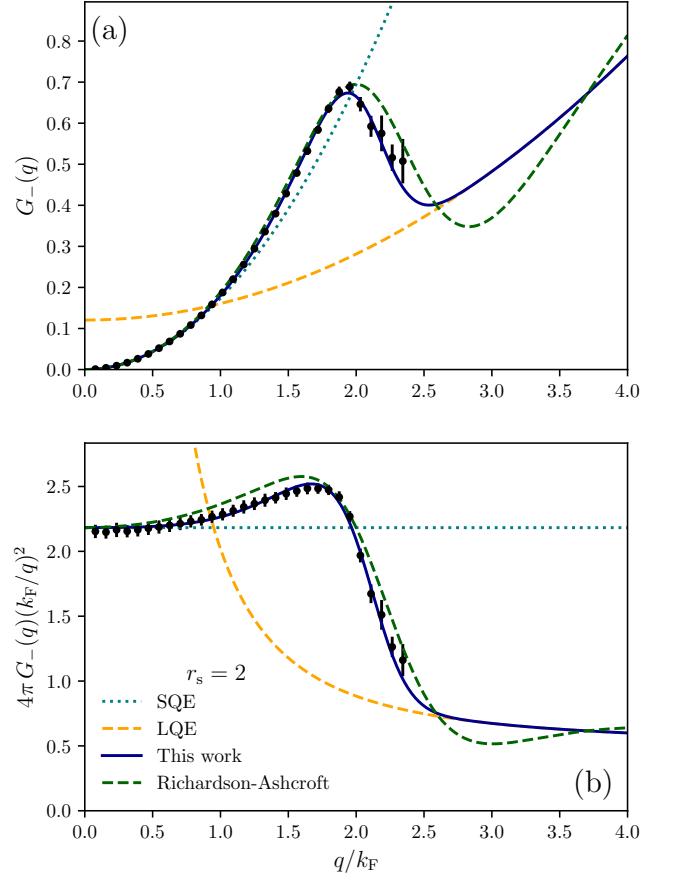
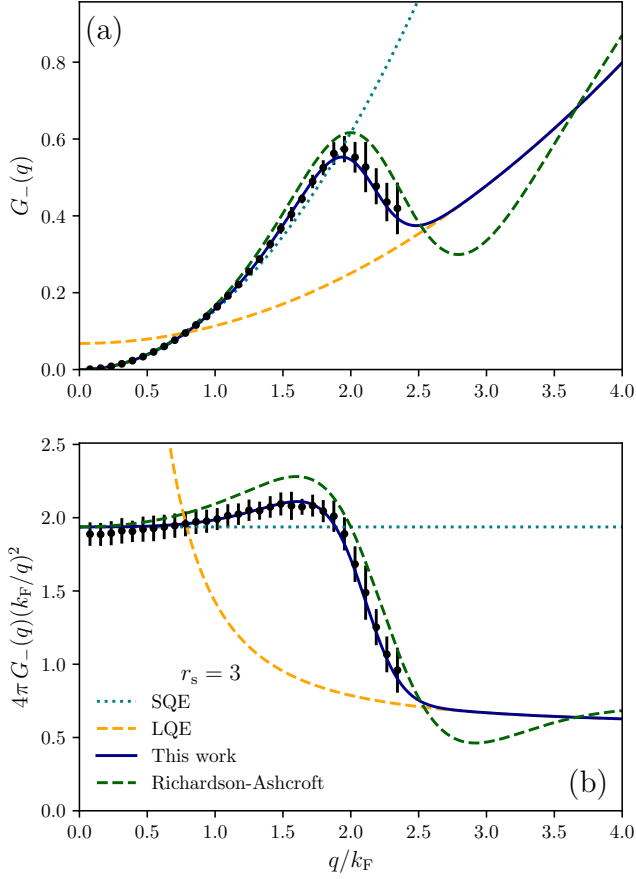
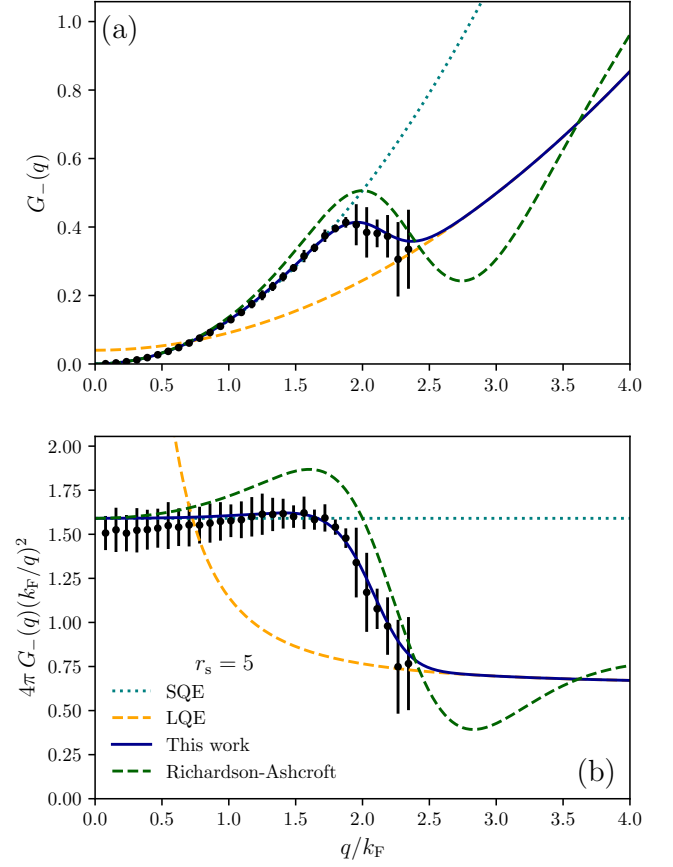


FIG. S9. Same as Fig. S8, but for $r_s = 2$.

FIG. S10. Same as Fig. S8, but for $r_s = 3$.FIG. S11. Same as Fig. S8, but for $r_s = 5$.

S3. QUALITY OF EXTRAPOLATION

This section presents the *predictions* of the model LFFs for the shapes of $G_{\pm}(q)$ at values of r_s for which they are not fitted. This gauges the quality of extrapolation and reliability of this model for jellium at any density.

For both $G_{\pm}(q)$, we show extrapolations to an extremely high density, $r_s = 0.1$ in Figs. S12 and S14, and to an extremely low density, $r_s = 100$ in Figs. S13 and S15.

A. Static density local field factor

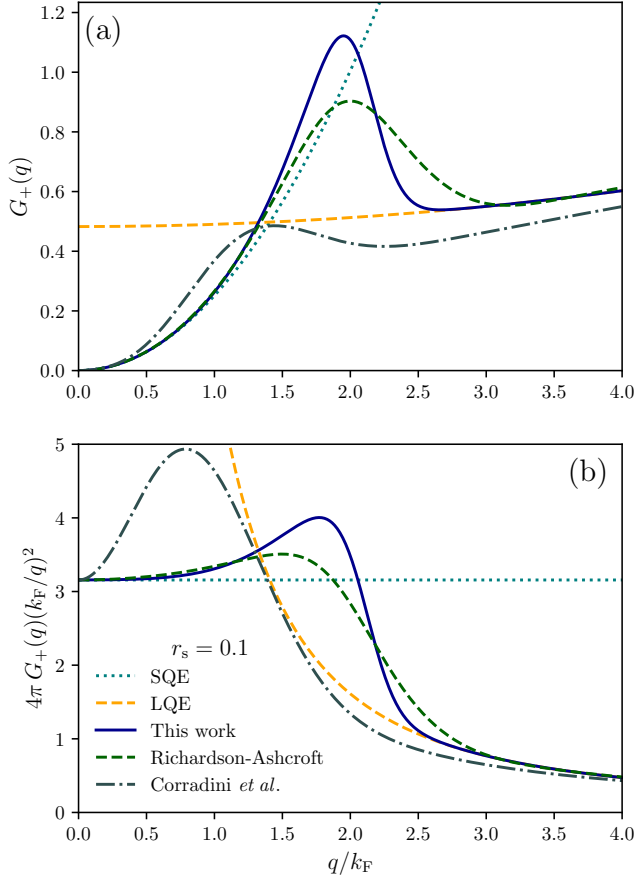


FIG. S12. Extrapolation of the model G_+ to $r_s = 0.1$. Panel (a) presents G_+ and (b) $4\pi G_+(k_F/q)^2 = k_F^2 f_{xc}(q)$. Also shown are the LFFs of Corradini *et al.* [6] (gray, dash-dotted), which is fitted to the data of Ref. [12], and of RA [8] (red, dashed). The small- q expansion (SQE) of Eq. (6) (orange, dotted) and large- q expansion (LQE) of Eq. (11) (green, dotted) are also shown.

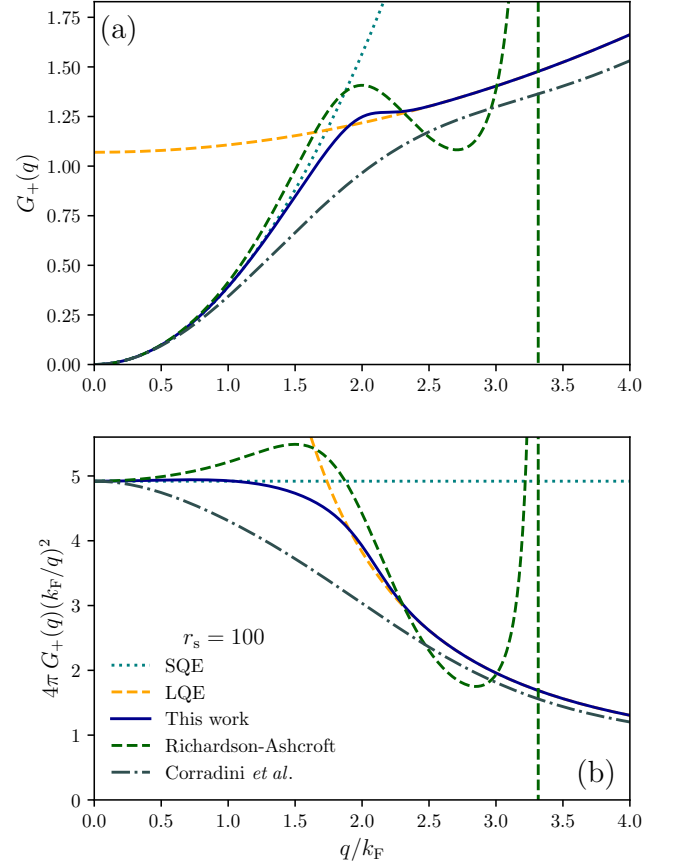


FIG. S13. Same as Fig. S12, but for $r_s = 100$.

B. Static spin local field factor

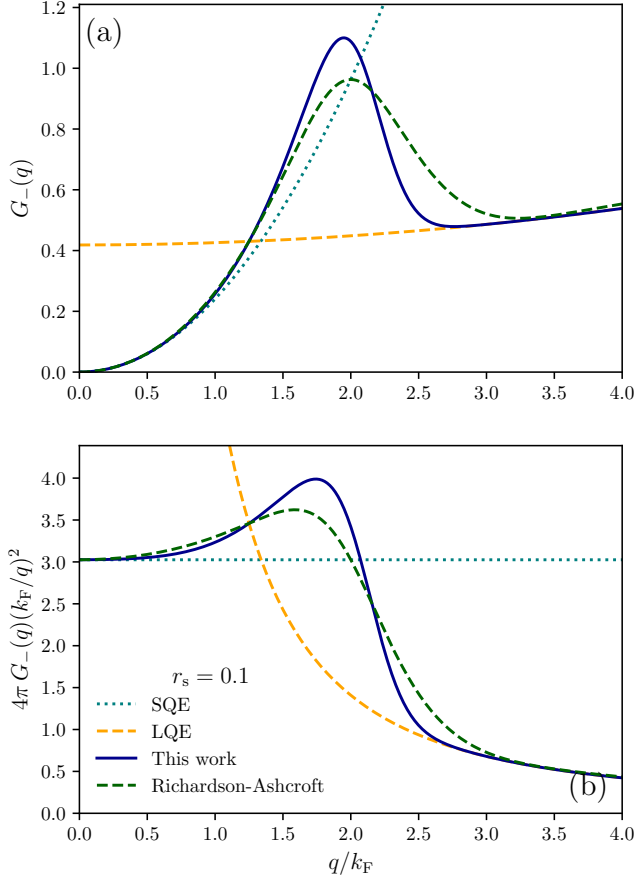


FIG. S14. Extrapolation of the model G_- to $r_s = 0.1$. Panel (a) presents G_- and (b) $4\pi G_-(k_F/q)^2 = k_F^2 f_{xc}(q)$. The RA expression for G_- [8] (red, dashed), the small- q expansion (SQE) of Eq. (6) (orange, dotted), and large- q expansion (LQE) of Eq. (11) (green, dotted) are also shown.

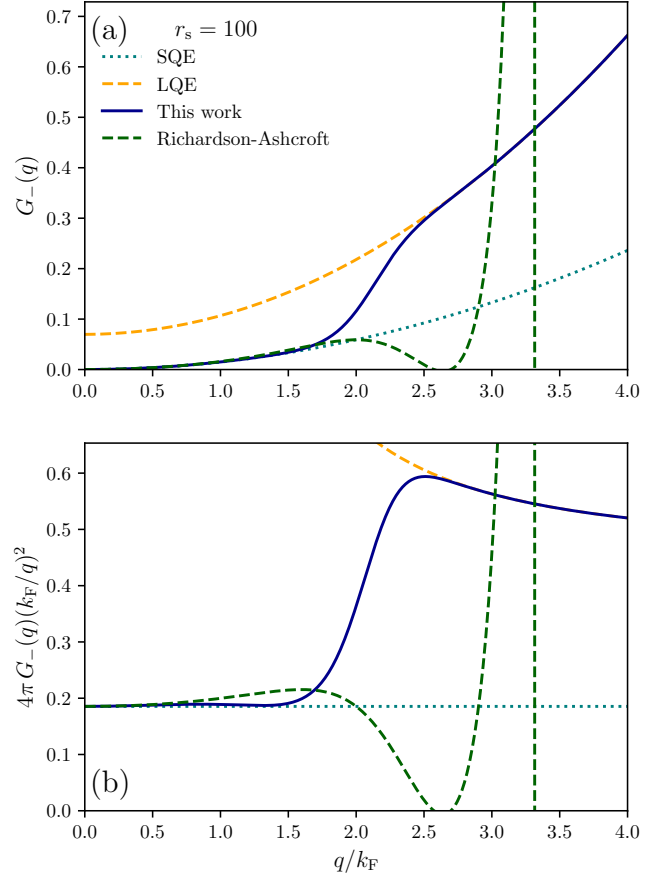


FIG. S15. Same as Fig. S14, but for $r_s = 100$.

S4. SURFACE PLOTS OF THE LOCAL FIELD FACTORS

This section presents surface plots of $G_+(r_s, q)$ as a function of q/k_F and r_s , with comparisons to the Corradini *et al.* LFF in Fig. S16, and to the Richardson-Ashcroft (RA) LFF in Fig. S17. The model of $G_-(r_s, q)$ developed here and the model of RA are compared in Fig. S18.

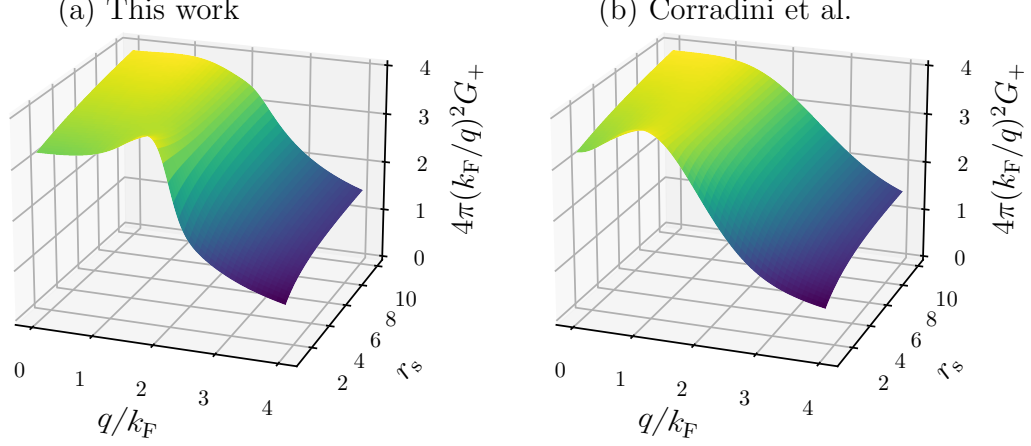


FIG. S16. Surface plot of (a) the model $4\pi G_+(r_s, q)(k_F/q)^2$ of this work and (b) of Corradini *et al.* [6]. Both are shown as functions of $0 \leq q/k_F \leq 4$ and in the metallic range $2 \leq r_s \leq 10$.

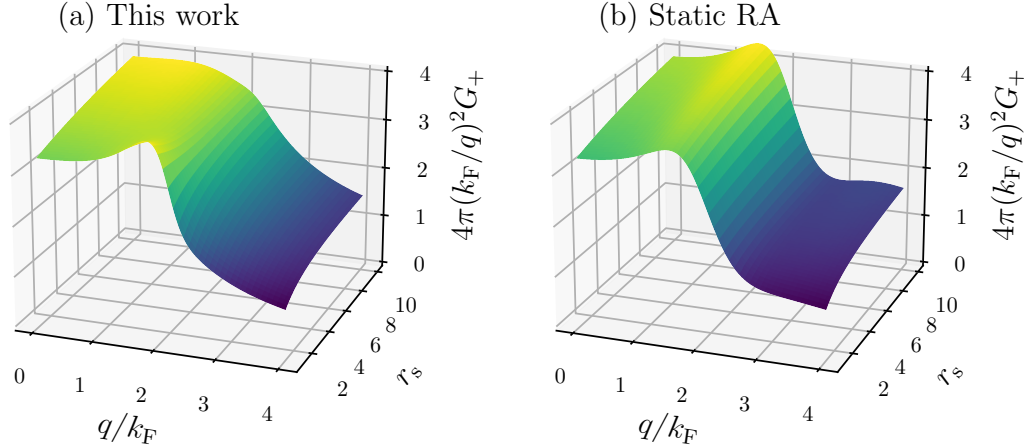


FIG. S17. Surface plot of (a) the model $4\pi G_+(r_s, q)(k_F/q)^2$ of this work and (b) of Richardson and Ashcroft (RA) [8]. Both are shown as functions of $0 \leq q/k_F \leq 4$ and in the metallic range $2 \leq r_s \leq 10$.

S5. COMPUTATION OF CORRELATION ENERGIES

To compute correlation energies per electron for a spin-unpolarized jellium, $\varepsilon_c(r_s, \zeta = 0)$, we use the standard coupling-constant integration [35]

$$\varepsilon_c(r_s, \zeta = 0) = -3 \int_0^\infty d\left(\frac{q}{k_F}\right) \int_0^1 d\lambda \int_0^\infty d\left(\frac{u}{k_F^2}\right) \frac{[\chi_0(q, iu)]^2 f_{\text{Hxc}}^{(\lambda)}(q, iu)}{1 - \chi_0(q, iu) f_{\text{Hxc}}^{(\lambda)}(q, iu)}. \quad (\text{S29})$$

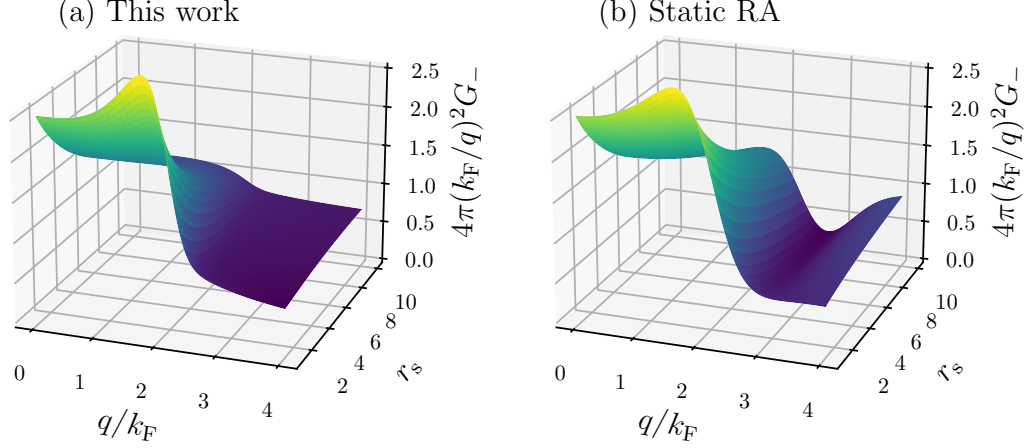


FIG. S18. Surface plot of (a) the model $4\pi G_-(r_s, q)(k_F/q)^2 G_-$ of this work and (b) of Richardson and Ashcroft (RA) [8]. Both are shown as functions of $0 \leq q/k_F \leq 4$ and in the metallic range $2 \leq r_s \leq 10$.

χ_0 is the non-interacting or Kohn-Sham response function. When evaluated for the UEG, it also known as the Lindhard function [2],

$$\chi_0(q, iu) = \frac{k_F}{2\pi^2} \left\{ \frac{z^2 - U^2 - 1}{4z} \ln \left[\frac{U^2 + (z+1)^2}{U^2 + (z-1)^2} \right] - 1 + U \arctan \left(\frac{1+z}{U} \right) + U \arctan \left(\frac{1-z}{U} \right) \right\}, \quad (\text{S30})$$

where $z = q/(2k_F)$ and $U \equiv u/(qk_F)$. $f_{\text{Hxc}}^{(\lambda)}$ is the sum of Hartree,

$$f_{\text{H}}(q) = \frac{4\pi}{q^2}, \quad (\text{S31})$$

and exchange-correlation kernels evaluated at the coupling-constant λ . From Ref. [35], we may obtain this expression from the coupling-constant scaled LFF

$$f_{\text{Hxc}}^{(\lambda)}(q, iu) = \frac{4\pi\lambda}{q^2} \left[1 - G_+ \left(\lambda r_s, \frac{q}{\lambda}, \frac{iu}{\lambda^2} \right) \right]. \quad (\text{S32})$$

Developing a method to reliably perform the three-dimensional integration needed in Eq. (S29) without combinatorial explosion is challenging. To do this, we first computed approximate random phase approximation (RPA) correlation energies by integrating up to two cutoffs, called $x_c \equiv q_c/k_F$ and $v_c \equiv u_c/k_F^2$,

$$\varepsilon_c^{\text{RPA}}(r_s) \approx -3 \int_0^{x_c} dx \int_0^1 d\lambda \int_0^{v_c} dv \frac{4\pi\lambda [\chi_0(q, iu)]^2 q^{-2}}{1 - 4\pi\lambda\chi_0(q, iu)/q^{-2}}. \quad (\text{S33})$$

As $G_+^{\text{RPA}} = 0$, the right- and left-hand-sides of Eq. (S33) become exactly equal in the limit that $x_c, v_c \rightarrow \infty$. These integrals were computed using globally-adaptive, Gauss-Kronrod quadrature. See the computational details of Refs. [36] and [10] for more details.

The cutoffs were adjusted to give agreement to within, ideally, 1% error of the PW92-parameterized RPA correlation energies [22]. These cutoffs were then approximately parameterized as continuous functions of r_s ,

$$x_c(r_s) \approx \begin{cases} c_{x0} + c_{x1}r_s, & r_s \leq 5 \\ c_{x0} + 5c_{x1} + c_{x2}(r_s - 5) + c_{x3}(r_s - 5)^2, & 5 < r_s \leq 60 \\ c_{x0} + 5c_{x1} + 55c_{x2} + 3025c_{x3} + c_{x4}(r_s - 60), & 60 < r_s \end{cases}, \quad (\text{S34})$$

with $c_{x0} = 3.928319$, $c_{x1} = 0.540168$, $c_{x2} = 0.042225$, $c_{x3} = 0.001810$, and $c_{x4} = 2.501585$. Analogously,

$$v_c(r_s) \approx \begin{cases} c_{v0} + c_{v1}r_s^{c_{v2}}, & r_s \leq 40 \\ c_{v0} + c_{v1}(40)^{c_{v2}} + (r_s - 40)^{c_{v3}}, & 40 < r_s \end{cases}, \quad (\text{S35})$$

r_s	$\varepsilon_c^{\text{RPA}}(r_s)$	$\varepsilon_c^{\text{PW-RPA}}(r_s)$	Percent Deviation (%)
0.1	-0.143815	-0.143819	0.00
0.5	-0.097155	-0.097221	0.07
1.0	-0.078631	-0.078741	0.14
2.0	-0.061651	-0.061797	0.24
3.0	-0.052619	-0.052774	0.29
4.0	-0.046673	-0.046827	0.33
5.0	-0.042343	-0.042491	0.35
10.0	-0.030549	-0.030661	0.37
20.0	-0.021288	-0.021367	0.37
40.0	-0.014385	-0.014454	0.48
60.0	-0.011300	-0.011367	0.59
80.0	-0.009472	-0.009542	0.74
100.0	-0.008236	-0.008311	0.90
120.0	-0.007345	-0.007413	0.93

TABLE S4. Comparison of the RPA correlation energies computed using the method described here, and with the Perdew-Wang approximation for the RPA correlation energy, PW-RPA [22]. The PW-RPA approximation is simply a parameterization of the accurate RPA data of Vosko, Wilk, and Nusair [24]. Percent deviations, $100\% \cdot (1 - \varepsilon_c^{\text{RPA}}/\varepsilon_c^{\text{PW-RPA}})$, are shown in the last column.

with $c_{v0} = 1.227277$, $c_{v1} = 5.991171$, $c_{v2} = 0.283892$, and $c_{v3} = 0.379981$.

To recover the error lost in using finite integration bounds, we then perform a set of coordinate remappings. Let $f(x)$ be a generic function of x , and $g(v)$ a generic function of v . Then the mappings used are

$$\int_0^\infty dx f(x) = \int_0^{x_c} dx f(x) + \int_0^{1/x_c} dt \frac{f(1/t)}{t^2} \quad (\text{S36})$$

$$\int_0^\infty dv g(v) = \int_0^{v_c} dv g(v) + \int_0^1 dw \frac{g(v_c - \ln(1-w))}{1-w}. \quad (\text{S37})$$

These mappings are, in principle, exact. For the range of $0 < x < x_c$, we use 100-point Gauss-Legendre quadrature, and for the range of $0 < t < 1/x_c$, we use 50-point Gauss-Legendre quadrature. The same number of points were used for the corresponding ranges of v and w , respectively. 100-point Gauss-Legendre quadrature was used for the coupling-constant, λ , integration. Table S4 shows that this method becomes asymptotically exact as $r_s \rightarrow 0$, and, in the metallic range $1 \leq r_s \leq 10$, gives generally negligible percent deviations from the Perdew-Wang parameterization of the RPA correlation energy, PW-RPA [22]. Indeed, for all $r_s \leq 120$, this method yields percent deviations less than 1% from PW-RPA.

S6. CORRECTED EXPRESSIONS FOR THE RICHARDSON-ASHCROFT LOCAL FIELD FACTORS

The work of Richardson and Ashcroft [8] is extremely important, as it is the first work to directly compute the individual LFFs G_s , G_a , and G_n at a range of wavevectors, frequencies, and densities. Moreover, they provided sensible parameterizations of these functions that are unfortunately hindered by typographical errors, as realized by Lein *et al.* [35]. We provide further corrections here. The density and spin LFFs are computed as

$$G_+(r_s, q, \omega) = G_s(r_s, q, \omega) + G_n(r_s, q, \omega) \quad (\text{S38})$$

$$G_-(r_s, q, \omega) = G_a(r_s, q, \omega) + G_n(r_s, q, \omega). \quad (\text{S39})$$

As before, $q > 0$ is a wavevector, and ω is a complex-valued frequency. The following dimensionless variables are used in the Richardson-Ashcroft work

$$z = q/(2k_F) \quad (\text{S40})$$

$$u = \frac{1}{2k_F^2} \text{Im } \omega. \quad (\text{S41})$$

A few r_s -dependent functions are used to define the low- and high-frequency regimes of the LFFs, $\lambda_i^{(j)}$, where $i = s, a, n$ and $j = 0, \infty$. Richardson and Ashcroft parameterized the relationship between the $u \rightarrow 0$ behaviors of G_a and G_n as

$$\frac{\lambda_n^{(0)}}{\lambda_n^{(0)} + \lambda_a^{(0)}} \approx \frac{-(0.11)r_s}{1 + (0.33)r_s} \equiv \mathcal{F}(r_s). \quad (\text{S42})$$

Their sum is rigorously computed using Eq. (RA:39) of Ref. [35],

$$\lambda_n^{(0)} + \lambda_a^{(0)} = 1 - 3 \left(\frac{2\pi}{3} \right)^{2/3} r_s \frac{\partial^2 \varepsilon_c}{\partial \zeta^2}(r_s, 0), \quad (\text{S43})$$

where $\varepsilon_c(r_s, \zeta)$ is in *Hartree* units, and not Rydberg units as in Ref. [8] or Eq. (RA:39) of Ref. [35]. Thus

$$\lambda_n^{(0)} = \mathcal{F}(r_s) \left[1 - 3 \left(\frac{2\pi}{3} \right)^{2/3} r_s \frac{\partial^2 \varepsilon_c}{\partial \zeta^2}(r_s, 0) \right], \quad (\text{S44})$$

$$\lambda_a^{(0)} = \frac{1 - \mathcal{F}(r_s)}{\mathcal{F}(r_s)} \lambda_n^{(0)}. \quad (\text{S45})$$

The $u \rightarrow 0$ limit of the spin-symmetric, noninteracting LFF is then

$$\lambda_s^{(0)} = -\lambda_n^{(0)} + 1 + \frac{2\pi}{3} a_x r_s^2 \frac{\partial \varepsilon_c}{\partial r_s}(r_s, 0) - \frac{\pi}{3} a_x r_s^3 \frac{\partial^2 \varepsilon_c}{\partial r_s^2}(r_s, 0) \quad (\text{S46})$$

again with $\varepsilon_c(r_s, \zeta)$ in Hartree. $a_x = [4/(9\pi)]^{1/3}$ is the inverse of the factor that relates the Fermi momentum to the Wigner-Seitz radius, $r_s = (a_x k_F)^{-1}$.

Although not defined explicitly in Ref. [8], the high-frequency limit of the spin-antisymmetric, noninteracting LFF is

$$\lambda_a^{(\infty)} = \frac{2g(r_s) - 1}{3}, \quad (\text{S47})$$

where again, $g(r_s)$ is the on-top pair distribution function. The high-frequency limit of the occupation number LFF is given as

$$\lambda_n^{(\infty)} = 6\pi a_x r_s \frac{\partial}{\partial r_s} [r_s \varepsilon_c(r_s, 0)], \quad (\text{S48})$$

and the corresponding limit of the spin-symmetric, noninteracting LFF from Eq. (RA:39) of Ref. [35],

$$\lambda_s^{(\infty)} = \frac{3}{5} - \frac{4\pi a_x}{5} \left[r_s^2 \frac{\partial \varepsilon_c}{\partial r_s}(r_s, 0) + 2r_s \varepsilon_c(r_s, 0) \right]. \quad (\text{S49})$$

Finally, we give the expression for the spin-symmetric, noninteracting LFF as

$$\gamma_s \equiv \frac{9}{16[1 - g(r_s)]} \lambda_s^{(\infty)} + \frac{4\alpha_s - 3}{4\alpha_s} \quad (\text{S50})$$

$$a_s(u) = \lambda_s^{(\infty)} + \frac{\lambda_s^{(0)} - \lambda_s^{(\infty)}}{1 + (\gamma_s u)^2} \quad (\text{S51})$$

$$c_s(u) = \frac{3\lambda_s^{(\infty)}}{4[1 - g(r_s)]} - (1 + \gamma_s u)^{-1} \left[\frac{4}{3} - \frac{1}{\alpha_s} + \frac{3\lambda_s^{(\infty)}}{4[1 - g(r_s)]} \right] \quad (\text{S52})$$

$$b_s(u) = a_s(u) \left\{ 3a_s(u)(1 + u)^4 - \frac{8}{3}[1 - g(r_s)](1 + u)^3 - 2c_s(u)[1 - g(r_s)](1 + u)^4 \right\}^{-1} \quad (\text{S53})$$

$$G_s(z, iu) = z^2 \frac{a_s(u) + 2[1 - g(r_s)]b_s(u)z^6/3}{1 + c_s(u)z^2 + b_s(u)z^8}. \quad (\text{S54})$$

$\alpha_s = 0.9$ is a fit parameter.

Likewise, the spin-antisymmetric, noninteracting LFF is parameterized as

$$\gamma_a = \frac{9}{8}\lambda_a^{(\infty)} + \frac{1}{4}, \quad (\text{S55})$$

$$a_a(u) = \lambda_a^{(\infty)} + \frac{\lambda_a^{(0)} - \lambda_a^{(\infty)}}{1 + (\gamma_a u)^2} \quad (\text{S56})$$

$$c_a(u) = \frac{3}{2}\lambda_a^{(\infty)} - [1 + (\gamma_a u)^2]^{-1} \left[\frac{1}{3} + \frac{3}{2}\lambda_a^{(\infty)} \right] \quad (\text{S57})$$

$$\beta_a(u) = \frac{4g(r_s) - 1}{3} - \lambda_a^{(\infty)} \frac{(\gamma_a u)^2}{1 + (\gamma_a u)^2} \quad (\text{S58})$$

$$b_a(u) = a_a(u) [3a_a(u)(1+u)^4 - 4\beta_a(u)(1+u)^3 - 3c_a(u)\beta_a(u)(1+u)^4]^{-1} \quad (\text{S59})$$

$$G_a(z, iu) = \lambda_a^{(\infty)} \frac{(\gamma_a u)^2}{1 + (\gamma_a u)^2} + z^2 \frac{a_a(u) + b_a(u)\beta_a(u)z^6}{1 + c_a(u)z^2 + b_a(u)z^8}. \quad (\text{S60})$$

Last, the occupation number LFF is parameterized as

$$a_n(u) = \lambda_n^{(\infty)} + \frac{\lambda_n^{(0)} - \lambda_n^{(\infty)}}{1 + (\gamma_n u)^2} \quad (\text{S61})$$

$$c_n(u) = \frac{3\gamma_n u}{(1.18)(1 + \gamma_n u)} - [1 + (\gamma_n u)^2]^{-1} \left[\frac{3\lambda_n^{(0)} + \lambda_n^{(\infty)}}{3\lambda_n^{(0)} + 2\lambda_n^{(\infty)}} + \frac{3\gamma_n u}{(1.18)(1 + \gamma_n u)} \right] \quad (\text{S62})$$

$$d_n(u) = a_n(u) + \lambda_n^{(\infty)} + \frac{2}{3}\lambda_n^{(\infty)}c_n(u)(1 + \gamma_n u) \quad (\text{S63})$$

$$b_n(u) = -\frac{3}{2\lambda_n^{(\infty)}(1 + \gamma_n u)^2} \left\{ d_n(u) + \left[d_n(u)^2 + \frac{4}{3}\lambda_n^{(\infty)}a_n(u) \right]^{1/2} \right\} \quad (\text{S64})$$

$$G_n(z, iu) = z^2 \frac{a_n(u) - \lambda_n^{(\infty)}b_n(u)z^4/3}{1 + c_n(u)z^2 + b_n(u)z^4}. \quad (\text{S65})$$

$\gamma_n = 0.68$ is another fit parameter.